Hypersonic Boundary-Layer Transition on Blunted Cones at Angle of Attack

Pedro Paredes,*
National Institute of Aerospace, Hampton, VA 23666, USA

Anton Scholten, †
North Carolina State University, Raleigh, NC 27695, USA

Meelan M. Choudhari,‡ Fei Li,§
NASA Langley Research Center, Hampton, VA 23681, USA

Experimental studies of cones at several high-speed facilities have demonstrated that, for small nosetip bluntness, transition onset over a circular cone moves upstream along the leeward side and downstream along the windward side, but this trend may be reversed at large bluntness values, where transition onset moves downstream along the leeward side and upstream along the windward side. A theoretical and numerical investigation is performed to characterize the effects of nose bluntness on disturbance amplification over the circular cone for several angles of attack, with the goal of understanding the potential physical mechanisms behind the experimental observations. The three-dimensional laminar basic states over a 1.5 m long, 7-degree half-angle cone with 9.525 mm nosetip radius are computed for selected angles of attack values and freestream conditions that are selected to match the Mach 10 experiments conducted within the Hypervelocity Wind Tunnel 9 at the Arnold Engineering Development Complex (AEDC). The solutions at a freestream unit Reynolds number of 17.1 million per meter are used to perform detailed instability analyses for angles of attack equal to 0, 1, 3, and 5 degrees. Results indicate that the linear amplification of stationary crossflow waves along inflection lines may begin to influence transition along the acreage of the cone for angles of attack equal to or larger than 5 degrees. The measured trend in transition front with respect to increasing angle of attack is found to be consistent with the predicted increase in the amplification factors for Mack mode disturbances along the streamline trajectories. The increase in Mack mode amplification along the windward ray for higher angles of attack is shown to be the result of a progressively earlier entropy-layer swallowing. Computations also indicate that the transition amplification factor along the windward ray is not constant and increases with the angle of attack and that the transition N-factors along the leeward ray are rather small. The nonmodal analysis for zero degrees angle of attack shows that entropy-layer disturbances with appreciably strong energy growth can coexist with Mack mode instabilities at the measured transition location.

Nomenclature

AoA	=	angle of attack, $^\circ$
E	=	total energy norm
f	=	disturbance frequency, s^{-1}
G	=	energy gain
h_t	=	total enthalpy, $kg \cdot m^2 \cdot s^{-2}$
h_ξ	=	streamwise metric factor
h_ζ	=	azimuthal metric factor

*Senior Research Engineer, Computational AeroSciences Branch, NASA LaRC. AIAA Senior Member
†Graduate Student, Department of Mechanical and Aerospace Engineering. AIAA Student Member
‡Research Scientist, Computational AeroSciences Branch. AIAA Fellow
§Research Scientist, Computational AeroSciences Branch.

m	=	azimuthal wavenumber, rad^{-1}
M	=	Mach number
N	=	Logarithmic amplification factor
$\hat{\mathbf{q}}$	=	vector of amplitude variables
$\check{\mathbf{q}}$	=	vector of disturbance function variables
$\bar{\mathbf{q}}$	=	vector of base flow variables
$\tilde{\mathbf{q}}$	=	vector of perturbation variables
Re_∞	=	freestream unit Reynolds number m^{-1}
R_c	=	local radius of an axisymmetric body at the axial station of interest, m
R_N	=	nose radius, m
T	=	temperature, K
T_w	=	wall temperature, K
(u, v, w)	=	streamwise, wall-normal, and azimuthal velocity components $\text{m} \cdot \text{s}^{-1}$
(x, y, z)	=	Cartesian coordinates
α	=	streamwise wavenumber, m^{-1}
β	=	spanwise wavenumber, m^{-1}
δ_h	=	boundary-layer thickness, m
δ_S	=	entropy-layer thickness, m
κ_ξ	=	streamwise curvature, m^{-1}
κ_ζ	=	spanwise curvature, m^{-1}
λ	=	spanwise wavelength, m
ω	=	disturbance angular frequency, s^{-1}
ρ	=	density, $\text{kg} \cdot \text{m}^{-3}$
(ξ, η, ζ)	=	streamwise, wall-normal, and spanwise coordinates, m
ϕ	=	azimuthal angle, rad
ΔS	=	entropy increment, $\text{kg} \cdot \text{m}^2 \cdot \text{s}^{-2} \cdot \text{K}^{-1}$
$\mathbf{M}$	=	energy weight matrix
Superscripts		
$*$	=	dimensional value
H	=	conjugate transpose
Subscript		
∞	=	freestream value
0	=	initial position
1	=	final position
T	=	transition location

I. Introduction

Laminar-turbulent transition of boundary-layer flows can have a strong impact on the performance of hypersonic vehicles because of their influence on the surface skin friction and aerodynamic heating. Therefore, the prediction and control of transition onset and the associated variation in aerothermodynamic parameters in high-speed flows are key issues for optimizing the performance of next-generation aerospace vehicles. Although many practical aerospace vehicles have blunt, hemispherical and ogival nose-tips, the mechanisms that lead to boundary-layer instability and transition on such geometries are not fully understood as yet. A detailed review of boundary-layer transition over sharp and blunt cones in a hypersonic freestream is given by Schneider [1]. As described therein, both experimental and numerical studies have shown that the modal growth of Mack-mode instabilities (or, equivalently, the so-called second-mode waves) is responsible for laminar-turbulent transition on sharp, axisymmetric cones at zero degrees angle of attack. Studies have also shown that increased nose-tip bluntness, e.g., a larger radius of the hemispherical or ogival nose-tip, leads to the formation of an entropy layer that can extend well beyond the nose-tip region [2]. This entropy layer has been shown to have a stabilizing effect on the amplification of Mack-mode instabilities, which is consistent with the observation that the onset of transition is displaced downstream as the nose bluntness is increased gradually from a sharp cone. However, while the boundary-layer flow continues to become more stable with increasing nose bluntness, experiments indicate that the downstream movement in transition slows down and eventually reverses when the nose bluntness exceeds a critical range [2].

Because of the failure of modal instability theory to predict the transition within the swallowing distance of the entropy layer [e.g., Refs. 3–6], nonmodal growth was proposed by Paredes et al. [7] as the potential basis for a physics-based model for the experimentally observed onset of transition. Results indicate that stationary disturbances that are initiated within the nose-tip vicinity can undergo relatively significant nonmodal amplification that increases with the nose-tip bluntness. This finding does not provide a definitive link between transient growth and the onset of transition, but is qualitatively consistent with the experimental observations that transition during the reversal regime on large bluntness configurations was highly sensitive to wall roughness, and additionally, was dominated by disturbances originating near the nose tip. However, transition at moderately-large bluntness can occur significantly downstream from the nose-tip, i.e., over the frustum of the cone [2]. For these moderately blunt conditions, experiments by Stetson [2] and Jewell et al. [8] indicated that uncontrolled nose-tip roughness did not influence the transition onset location, suggesting that unsteady freestream disturbances may play a role in initiating frustum transition over moderately-large bluntness cones. Computational analysis by Refs. [7, 9, 10] has shown significant nonmodal growth of both planar and oblique traveling disturbances that peak within the entropy layer and above the boundary-layer edge. The linear, nonmodal amplification of the energy norm associated with the nonstationary disturbances was lower than that for the three-dimensional stationary disturbances, but increased as the nose-tip bluntness was increased [10]. Therefore, Paredes et al. [10] suggested that nonstationary nonmodal traveling disturbances that peak within the entropy layer could lead to transition onset in the absence of appreciable modal instability amplification. Furthermore, Paredes et al. [11] demonstrated that, even though the linear nonmodal disturbances are primarily concentrated outside the boundary layer, their nonlinear interaction can generate stationary streaks that penetrate and amplify within the boundary layer, eventually inducing the onset of transition via the breakdown of these streaks.

The effect of the angle of attack on blunt cones at hypersonic speeds has been predominantly studied in experimental measurements [e.g., Refs. 5, 12–14]. A detailed review of the experimental measurements is presented by Schneider [1]. The experiments agree that the transition location experiences a different trend between small or negligible and large bluntness values. While the transition onset always moves upstream on the leeward side and downstream on the windward side for sharp cones with increasing angle of attack, the transition onset movement reverses for large bluntness values, becoming downstream on the leeward side and upstream on the windward side. The transition onset movement along the leeward side depends on the bluntness and is not always monotonic with angle of attack. The experiments conducted by Marineau et al. [5] and Moraru [15] in the Arnold Engineering Development Complex (AEDC) Hypervelocity Wind Tunnel 9 at Mach 10 with 1.5 m long, 7-degree half-angle, sharp and blunted cones agree with the trends of the previous data. Furthermore, the TSP and heat transfer measurements along the acreage show a monotonous transition front as a function of the azimuthal angle, which is not observed in the small-bluntness, cold-wall experiments at Mach 6 by Stetson [16] and Swanson and Schneider [17] or at Mach 7 by Willems et al. [18]. This might indicate a stabilizing effect of the entropy layer on the crossflow instability along the side of the cone.

The present paper investigates the effect of the bluntness on the modal and nonmodal instability characteristics of the boundary layer over a 7-degree half-angle cone with 9.525 mm nose radius that was tested in the AEDC Hypervelocity Wind Tunnel 9. The methodologies used to investigate the modal and nonmodal disturbances are summarized in Section II. Then, the laminar basic states at angles of attack equal to 0, 1, 3, and 5 degrees and the respective predictions from detailed instability analyses are presented in Section III. A summary and the concluding remarks are presented in Section IV.

II. Theory

In this section, we outline the methodology used for the analysis of disturbance amplification over the blunt cone configurations of interest. Following the work of Refs. [7, 10], we use the harmonic linearized Navier-Stokes equations (HLNSE) and the linear parabolized stability equations (PSE) frameworks to investigate both modal and nonmodal disturbances.

A. Governing Equations for Modal and Nonmodal Disturbances

The present work is focused on the boundary layers over axisymmetric bodies in a hypersonic flow. The freestream conditions and geometries are selected to match selected configurations from the AEDC experiments [5, 15] with variable bluntness, 7-degree half-angle cones. For this problem, the computational coordinates are defined as an orthogonal, body-fitted coordinate system, with (ξ, η, ζ) denoting the streamwise, wall-normal, and spanwise coordinates, respectively, and (u, v, w) representing the corresponding velocity components. Density and temperature are denoted

by ρ and T. The metric factors are defined as

$$h_\xi = 1 + \kappa_\xi \eta, \tag{1}$$

$$h_\zeta = (1 + \kappa_\zeta \eta)\frac{\lambda}{\lambda_0}, \tag{2}$$

where κ_ξ denotes the streamwise curvature, κ_ζ denotes the spanwise curvature, and λ/λ_0 denotes the prescribed evolution of the spanwise disturbance wavelength, normalized by the wavelength at a reference position.

Linear perturbations that are assumed to be harmonic in time can be written as

$$\tilde{\mathbf{q}}(\xi, \eta, \zeta, t) = \breve{\mathbf{q}}(\xi, \eta, \zeta) \exp\left[-\mathrm{i}\omega t\right] + \mathrm{c.c.}, \tag{3}$$

where c.c. denotes complex conjugate. The streamwise wavenumber is α and ω is the angular frequency of the perturbation. The Cartesian coordinates are represented by (x, y, z). The vector of perturbation variables is denoted by $\tilde{\mathbf{q}}(\xi, \eta, \zeta, t) = (\tilde{\rho}, \tilde{u}, \tilde{v}, \tilde{w}, \tilde{T})^T$ and the vector of disturbance functions is $\breve{\mathbf{q}}(\xi, \eta, \zeta) = (\breve{\rho}, \breve{u}, \breve{v}, \breve{w}, \breve{T})^T$. The vector of basic state variables is $\bar{\mathbf{q}}(\xi, \eta, \zeta) = (\bar{\rho}, \bar{u}, \bar{v}, \bar{w}, \bar{T})^T$. The disturbance functions $\breve{\mathbf{q}}(\xi, \eta, \zeta)$ satisfy the HLNSE. For two-dimensional or axisymmetric geometries at zero degrees angle of attack, or under the assumption of spanwise homogeneous flow, the basic state variables are independent of the spanwise or azimuthal coordinate and the perturbations can be assumed to be harmonic also in the spanwise direction, which lead to the following expression for the perturbation of Eq. (3),

$$\tilde{\mathbf{q}}(\xi, \eta, \zeta, t) = \breve{\mathbf{q}}(\xi, \eta) \exp\left[\mathrm{i}\left(\beta\zeta - \omega t\right)\right] + \mathrm{c.c.}, \tag{4}$$

where β is the spanwise wavenumber. For axisymmetric geometries at zero degrees angle of attack, the coordinate ζ denotes the azimuthal direction and the azimuthal wavenumber m is used. The spanwise homogeneous assumption has been found to provide approximate predictions of the amplification of crossflow and Mack mode disturbances along inflection lines and streamlines over a three-dimensional configuration [19–24].

The PSE approximation to the HLNSE is based on isolating the rapid phase variations in the streamwise direction via the disturbance ansatz

$$\breve{\mathbf{q}}(\xi, \eta) = \hat{\mathbf{q}}(\xi, \eta) \exp\left[\mathrm{i}\int_{\xi_0}^{\xi} \alpha(\xi')\,\mathrm{d}\xi'\right], \tag{5}$$

where the unknown, streamwise varying wavenumber $\alpha(\xi)$ is determined in the course of the solution by imposing an additional constraint

$$\int_\eta \hat{\mathbf{q}}^* \frac{\partial \hat{\mathbf{q}}}{\partial \xi}\, h_\xi\, h_\zeta\, \mathrm{d}\eta\, \mathrm{d}\zeta = 0, \tag{6}$$

where the amplitude functions $\hat{\mathbf{q}}(\xi, \eta) = (\hat{\rho}, \hat{u}, \hat{v}, \hat{w}, \hat{T})^T$ vary slowly in the streamwise direction in comparison with the phase term $\exp\left[\mathrm{i}\int_{\xi_0}^{\xi} \alpha(\xi')\,\mathrm{d}\xi'\right]$. Substituting Eq. (5) into the HLNSE and invoking scale separation between the streamwise coordinate and the other two directions to neglect the viscous terms with streamwise derivatives, the PSE are obtained. The assumption of homogeneous spanwise direction fails in regions where the spanwise gradients of the basic state variables are comparable to the wall-normal gradients. In these cases, the plane-marching PSE can be used to predict the linear amplification of the instability waves. In the plane-marching PSE approach the disturbance amplitude function of Eq. (5) depends on the three spatial directions, $\hat{\mathbf{q}}(\xi, \eta, \zeta)$, and the parabolic integration of the disturbance equations involves the solution of a two-dimensional partial differential equation system. A description of the theoretical and numerical details of the conventional PSE and plane-marching PSE methodologies are given by Refs. [25–27].

The onset of laminar-turbulent transition is estimated using the logarithmic amplification ratio, the so-called N-factor, relative to the lower bound location ξ_{lb} where the disturbance first becomes unstable,

$$N_E = -\int_{\xi_{lb}}^{\xi} \alpha_i(\xi')\,\mathrm{d}\xi' + 1/2 \ln\left[\hat{E}(\xi)/\hat{E}(\xi_{lb})\right], \tag{7}$$

where $\hat{E}$ denotes the energy norm of $\hat{\mathbf{q}}$. The energy norm is defined as

$$\hat{E}(\xi) = \frac{1}{L_\zeta}\int_\eta \hat{\mathbf{q}}(\xi, \eta, \zeta)^H \mathbf{M}_E \hat{\mathbf{q}}(\xi, \eta, \zeta)\, h_\xi\, h_\zeta\, \mathrm{d}\eta, \tag{8}$$

where $\mathbf{M}_E$ is the energy weight matrix and the superscript H denotes conjugate transpose. The positive-definite energy norm used here was derived by Chu [28] and used by Mack [29] and Hanifi et al. [30] for linear stability theory. This energy norm is defined as

$$\mathbf{M}_E = \text{diag}\left[\frac{\bar{T}(\xi,\eta)}{\gamma\bar{\rho}(\xi,\eta)M^2}, \bar{\rho}(\xi,\eta), \bar{\rho}(\xi,\eta), \bar{\rho}(\xi,\eta), \frac{\bar{\rho}(\xi,\eta)}{\gamma(\gamma-1)\bar{T}(\xi,\eta)M^2}\right]. \tag{9}$$

B. Optimal Growth Theory

The optimal initial disturbance, $\tilde{\mathbf{q}}_0$, is defined as the initial (i.e., inflow) condition at ξ_0 that maximizes the objective function, J, which is defined as a measure of disturbance growth over a specified interval $[\xi_0, \xi_1]$. The definition used in the present study corresponds to the energy gain $J = G_E$ that is defined as

$$G_E = \frac{E(\xi_1)}{E(\xi_0)}, \tag{10}$$

where E denotes the energy norm of $\tilde{\mathbf{q}}$.

The variational formulation of the problem to determine the maximum of the objective functional J leads to an optimality system [10, 31], which is solved in an iterative manner, starting from a random solution at ξ_0 that must satisfy the boundary conditions. The HLNSE are used to integrate $\tilde{\mathbf{q}}$ up to ξ_1, where the final optimality condition is used to obtain the initial condition for the backward adjoint equations integration. At ξ_0, the adjoint solution is used to calculate the new initial condition for the forward integration with the initial optimality condition. The iterative procedure continues until the value of G has converged within a specified tolerance, which was set to 10^{-4} during the present computations.

C. Discretization and Boundary Conditions

Stable high-order finite-difference schemes [32, 33] of sixth order are used for discretization of the stability equations on the nonuniform grid along the the wall-normal direction. For the HLNSE, PSE, and plane-marching PSE results presented here, the wall-normal direction is discretized with $N_\eta = 201$, with the nodes being clustered toward the wall. The spanwise direction is also discretized with $N_\zeta = 201$ for the plane-marching PSE analysis of the leeward side of the cone at angle of attack. The discretized PSE and plane-marching PSE are integrated along the streamwise coordinate by using second-order backward differentiation. The HLNSE are discretized along the streamwise coordinate with centered, fourth-order finite differences. The number of discretization points in both directions was varied in selected cases to ensure the numerical convergence of the results.

No-slip, isothermal boundary conditions are used at the wall, i.e., $\hat{u} = \hat{v} = \hat{w} = \hat{T} = 0$. The farfield boundary is set just below the shock layer and, unless indicated otherwise, the amplitude functions are forced to decay at the farfield boundary by imposing the Dirichlet conditions $\hat{\rho} = \hat{u} = \hat{w} = \hat{T} = 0$. The plane-marching PSE analysis of the leeward side uses symmetric and antisymmetric boundary conditions at the leeward ray [34] and the amplitude functions are allowed to decay far from the leeward side by imposing a sponge region and Dirichlet conditions. The wall-normal and spanwise domain sizes were varied in selected cases to ensure the convergence of the results.

III. Results

This section begins with the presentation of the laminar Navier-Stokes solutions for the three-dimensional boundary-layer flows over a blunt $R_N^* = 9.525$ mm, 7° half-angle cone at angles of attack of 0°, 1°, 3°, and 5°, respectively, in a hypersonic freestream. Next, we present the modal instability analysis for stationary crossflow vortices developing along inflection lines spanning the surface of the cone, Mack mode instabilities along streamline trajectories, and the instability modes of the azimuthally localized vortex structure centered along the leeward ray of the selected configurations. Finally, the nonmodal, optimal growth characteristics of the boundary-layer flow are investigated for the single case of the zero degrees angle of attack configuration.

A. Laminar Boundary-Layer Flow

The flow configurations are selected to match the experiments in the Air Force AEDC Hypervelocity Wind Tunnel No. 9 (Tunnel 9) as described by Marineau et al. [5]. This facility is a hypersonic, nitrogen gas, blowdown wind tunnel

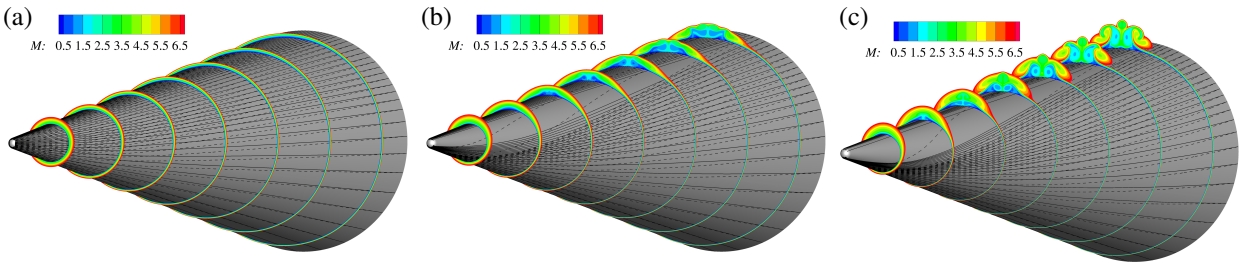

Fig. 1 Three-dimensional view of Mach number contours of the laminar boundary layer over a 7° cone with $R_N^* = 9.525$ mm at an angle of attack of (a) 1°, (b) 3°, and (c) 5°. The contours are shown at selected axial locations from $x = 0.2$ m to $x = 1.4$ m with constant increments of 0.2 m. The black solid and dashed lines correspond to the streamlines and inflection lines, respectively.

with interchangeable nozzles that allow for testing at Mach numbers of 7, 8, 10, and 14 over a 0.177×10^6 m^{-1} to 158.8×10^6 m^{-1} unit Reynolds number range. A detailed description of the facility can be found in Ref. [5]. The blunt cones used in the experiments had a base diameter of 15 in. (0.381 m) and interchangeable nose tips with radius of 0.152 mm to 50.80 mm. The working fluid is nitrogen at a relatively low temperature and pressure. Thus, the effects of chemistry and molecular vibration are omitted from the calculations.

The basic states corresponding to the laminar basic states over the selected configurations are computed by using a second-order accurate algorithm as implemented in the finite-volume compressible Navier-Stokes flow solver VULCAN-CFD* [35]. The VULCAN-CFD solution is based on the full Navier-Stokes equations and uses the solver's built-in capability to iteratively adapt the computational grid to the shock. The Keyes' law for diatomic Nitrogen [36] is used to calculate the viscosity as a function of temperature. The freestream conditions are selected to replicate those of the experiments, i.e., Mach 9.79 flow with a unit Reynolds number of 17.1×10^6 m^{-1}, freestream temperature of $T_\infty^* = 51.0$ K and an isothermal wall temperature of $T_w^* = 300$ K. The computational grid solves half of the geometry and imposes symmetry conditions along the windward and leeward planes. The grid is composed of a nosetip block and a frustum block to avoid the nosetip axis singularity. Sufficient clustering of points next to the cone surface allowed adequate resolution for the thickness of the boundary layer. Solutions were calculated for a medium grid with block sizes of $65 \times 129 \times 353$ and $961 \times 257 \times 353$ nodes, i.e., total number of nodes equal to $n_t \approx 90^6$, and fine grid with $97 \times 193 \times 529$ and $1441 \times 385 \times 529$ nodes, i.e., $n_t \approx 303^6$. The following results correspond to the medium grid for the $AoA = 1°$ case and fine grid for the $AoA = 3°$ and 5° cases. Selected results with the medium grid for the $AoA = 3°$ case are used to demonstrate the results are insensitive to the grid resolution.

The Mach number distributions corresponding to the three-dimensional laminar boundary-layer flow solutions for angles of attack of 1°, 3°, and 5° are shown in Fig. 1. A total of 32 streamlines and 32 inflection lines based on the velocity field at the generalized inflection points of the crossflow velocity profile [22] are also shown. The divergence of the streamlines from the windward side to the leeward side leads to the thickening of the boundary layer along the acreage of the cone. Figure 1 shows how a vortical structure is formed along the leeward side. As the angle of attack is increased, a detached three-dimensional shear layer forms and can sustain the growth of streak instabilities [34, 37, 38]. Furthermore, the angle between the inflection lines and the streamlines also increases with the angle of attack, which suggests the higher amplification of crossflow waves.

The evolution of the boundary-layer and entropy-layer thicknesses along the windward and leeward rays is plotted in Figs. 2(a) and 2(b), respectively, for the selected configurations. The boundary-layer edge, δ_h, is defined as the wall-normal position where $h_t/h_{t,\infty} = 0.995$, with h_t denoting the total enthalpy, i.e., $h_t = h + 0.5(\bar{u}^2 + \bar{v}^2 + \bar{w}^2)$, where $h = c_p\bar{T}$ is the static enthalpy. An increase in the angle of attack reduces the boundary-layer thickness and the entropy-layer height along the windward ray. An upstream movement of the entropy-layer swallowing location is observed as the angle of attack is increased, which is expected to result in an earlier onset of Mack mode amplification. Due to the formation of the vortical structure along the leeward side, the boundary layer thickness along the leeward ray is substantially higher as seen in Fig. 2(b).

*visit `http://vulcan-cfd.larc.nasa.gov` for further information about the VULCAN-CFD solver

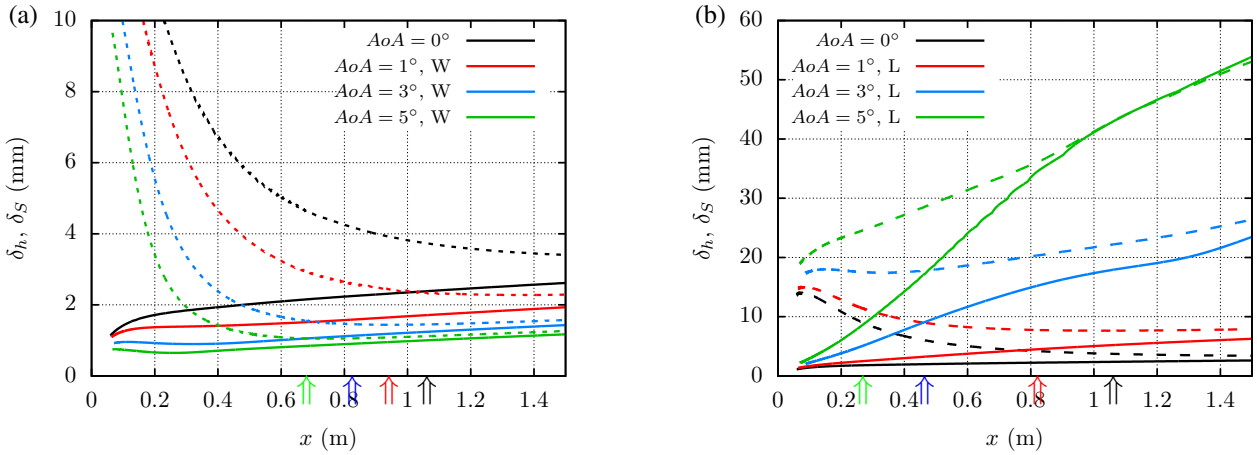

Fig. 2 Streamwise evolution of boundary-layer thickness (δ_h, solid lines) and entropy-layer thickness (δ_S, dashed lines) of the laminar boundary-layer flows over the selected configurations along the (a) windward and (b) leeward rays. The vertical arrows under the horizontal axis indicate the transition locations measured with thermocouples [5].

B. Linear Modal Analysis

Experimental measurements and theoretical predictions based on PSE have confirmed that laminar-turbulent transition for the sharp cone at zero degrees angle of attack and the same freestream conditions is driven by the modal growth of planar Mack-mode instabilities [5, 15]. For the selected nose radius of R^*_N = 9.525 mm and freestream conditions of M_∞ = 9.79 and Re_∞ = 17.1 m^{-1}, the wall-pressure disturbance measurements and PSE results show the incipient growth of Mack mode disturbances just upstream of the measured transition location. The predicted N-factor at the measured transition location is approximately N = 1.5, which appears to be too low to cause transition onset even within a conventional, i.e., noisy facility. The measurements of transition location via temperature sensitive paint (TSP) and thermocouples (TC) at the selected angles of attack showed upstream movements of the transition location along both windward and leeward sides for the present geometry. However, the transition front presented by Marineau et al. [5] up to AoA = 3° do not indicate the influence of crossflow disturbances along the side of the cone between the windward and leeward sides. To establish the instability characteristics of the selected configurations, the linear amplification of stationary crossflow and Mack mode disturbances is calculated with PSE along the inflection lines and streamlines, respectively, as shown in Fig. 1. Because of the strong crossplane gradients associated with the three-dimensional vortical structure along the leeward ray, the instability characteristics in that region are studied by using the plane-marching PSE.

1. Stationary Crossflow

The linear amplification characteristics of stationary crossflow disturbances in the boundary-layer flow over the selected configurations at angles of attack have been computed with linear PSE that accounts for the leading-order nonparallel and surface curvature effects. The PSE are integrated along 32 inflection lines along the surface of the cone. The local streamwise direction of the inflection lines are defined such that the generalized inflection point of the crossflow velocity profile coincides with a zero of the same profile. Furthermore, similar to Ref. [22], the variation of spanwise wavelength based on the diffluence of the inflection lines is included in the PSE analysis.

Figure 3 shows the amplification of stationary crossflow instability in terms of the N-factor envelope along the surface of the cone at AoA = 3° and AoA = 5°. Although not shown here, the maximum crossflow N-factor for the AoA = 1° is predicted to be lower than N_E = 3 by the end of the cone, which is deemed to be small enough to rule out the stationary crossflow vortices as the dominant cause for boundary layer transition. The vertical axis in the figure corresponds to the circumferential distance computed on the basis of the local radius R_c and angle ϕ with respect to the windward ray. The comparison of the N-factor results based on the medium and fine grids, respectively, as shown in Fig. 3(a) for the AoA = 3° case confirms the convergence of the results with the selected grids. The N-factor values increase from the windward symmetry plane, where the crossflow velocity is zero, maximize at an azimuthal angle that increases with axial location, and decrease toward the leeward side. The measured transition locations do not show

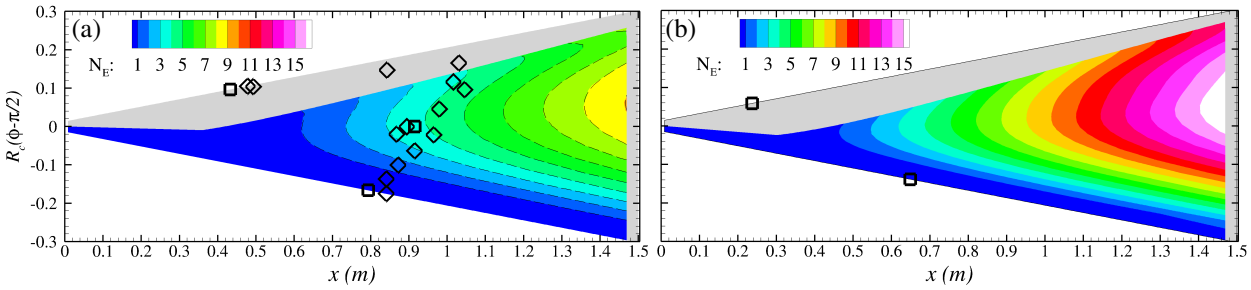

Fig. 3 N-factor contours of stationary crossflow instability computed with PSE along inflection lines for (a) $AoA = 3°$ and (b) $5°$. The open symbols denote the measured transition locations with TC (□) and TSP (⋄). The dashed lines of subfigure (a) denote the N-factor isolines corresponding to the medium grid while the colors correspond to the fine grid.

correlation with the N-factor contours for $AoA = 3°$. However, the maximum crossflow N-factor values at the transition locations are found to be lower than $N_E = 5$, and, therefore, are deemed too low to affect natural transition. The increase of the angle of attack from 3° to 5° leads to a notable increase in the crossflow N-factor values up to $N_E = 16$ by the end of the cone. Therefore, crossflow instability could potentially affect transition for $AoA \geq 5°$. However, the measured transition front across the azimuthal direction is not available for the $AoA = 5°$ condition. The crossflow results near the leeward side are not included in Fig. 3 because the complex vortical structure that forms over the leeward side prevents the accurate integration of the inflection lines and PSE. The plane-marching PSE is used instead to study the instability characteristics over the leeward side.

2. Mack Mode

The Mack mode instability amplification is calculated with linear PSE along 32 streamlines that cover the surface of the selected configurations from the windward to the leeward sides. Figure 4 shows the N-factor envelope of planar Mack mode waves along the streamlines over the surface of the cone at the selected angles of attack. The corresponding disturbance frequency of the Mack mode waves is shown in Fig. 5. Similar to the crossflow N-factor results of Fig. 3(a), the comparison of the N-factor and corresponding disturbance frequency results with the medium and fine grids shown in Figs. 4(c) and 5(c) for $AoA = 3°$ confirms the convergence of the results with the selected grids. The Mack mode waves are destabilized along the windward side as a consequence of the upstream movement of the entropy-layer swallowing location with an increase in the angle of attack as shown in Fig. 2. Figure 4 also shows how the N-factor at transition location monotonically increases with the angle of attack from $N_E = 1.5$ for $AoA = 0°$ to $N_E = 7$ for $AoA = 5°$. As one moves from the windward to the leeward symmetry plane, the accompanying shift in transition location approximately follows the locus of a constant Mack mode N-factor up to a certain distance from the leeward side, where a significantly earlier onset of transition within the localized vortical structure leads to the formation of a narrow turbulent wedge centered on the leeward ray. Figure 5 shows the increase of the leading Mack mode frequencies along the windward side as the angle of attack increases due to the boundary layer thickness reduction (Fig. 2). The gradual increase in boundary layer thickness toward the leeward side leads to a decrease in the disturbance frequency values. Similar to the crossflow results, the Mack mode results near the leeward side are not included for the $AoA = 3°$ and 5° in Figs. 4-5(c) and 4-5(d), respectively, because the complex vortical structure that forms over the leeward side prevent the accurate integration of the streamlines and PSE. The plane-marching PSE is used in the following subsection to study the instability characteristics over the leeward side.

3. Leeward Side

The vortical structure that forms over the leeward side as the angle of attack is increased (Fig. 1) leads to strong azimuthal gradients that prevents the accurate prediction of the instability characteristics with conventional PSE. Therefore, the plane-marching PSE are used to study the linear modal instabilities supported by the vortical structure, because they do not invoke the homogeneous spanwise assumption and are able to fully account for the three-dimensionality of the flow solution and disturbances.

The stability analysis for the selected configurations showed that the symmetric Mack mode waves that begin to

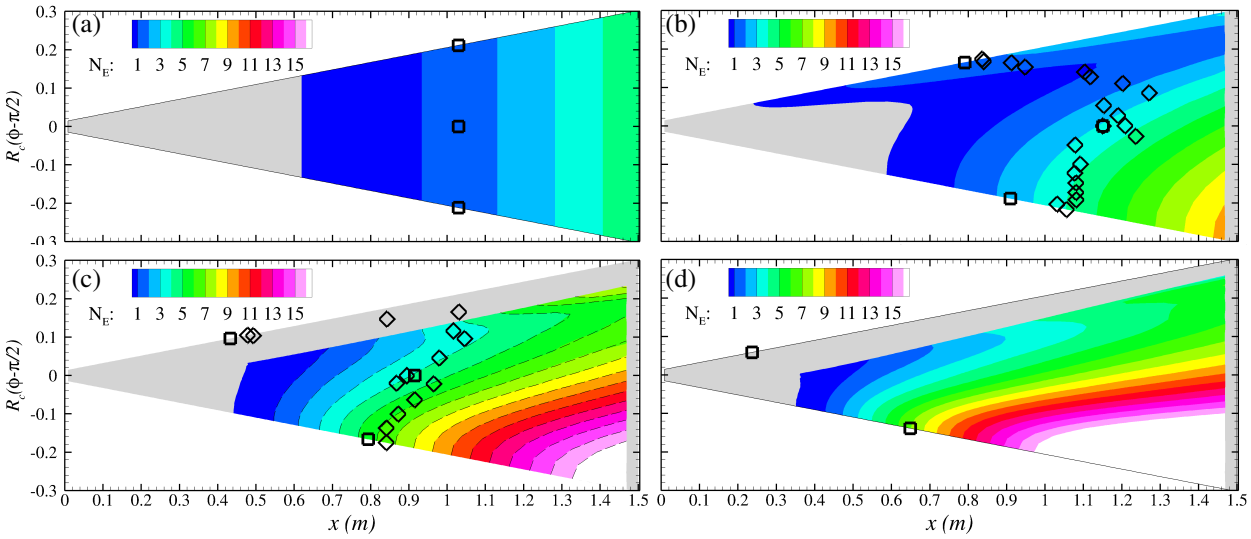

Fig. 4 *N*-factor envelope contours of Mack mode instability computed with PSE along streamlines for **(a)** $AoA = 0°$, **(b)** 1°, **(c)** 3°, and **(d)** 5°. The open symbols denote the measured transition locations with TC (□) and TSP (◇). The dashed lines of subfigure (c) denote the *N*-factor isolines corresponding to the medium grid while the colors correspond to the fine grid.

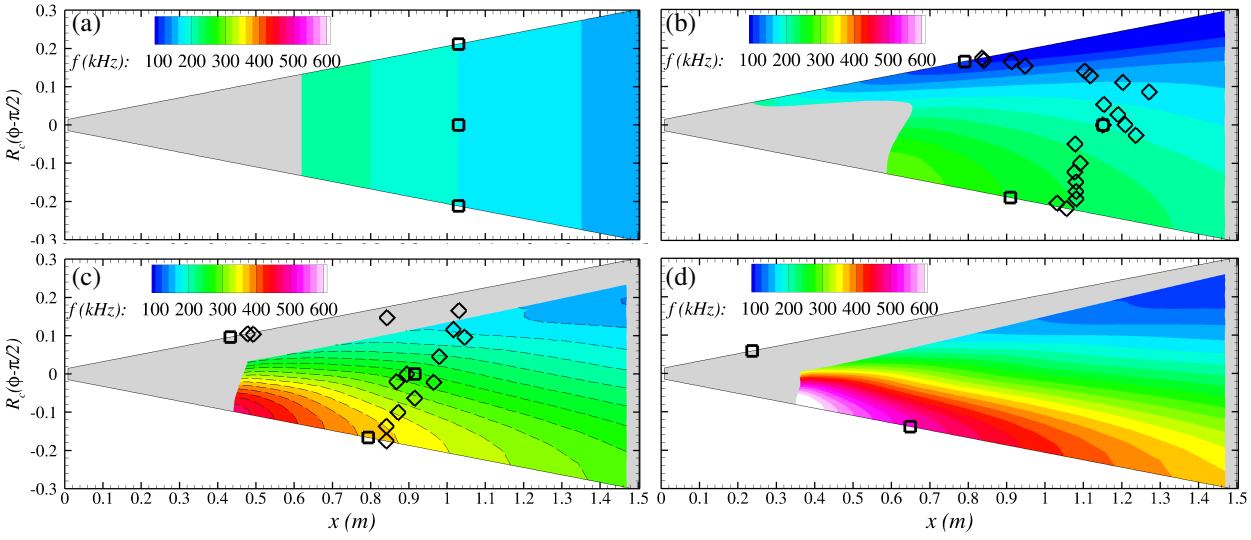

Fig. 5 Disturbance frequency contours of Mack mode instability computed with PSE along streamlines for **(a)** $AoA = 0°$, **(b)** 1°, **(c)** 3°, and **(d)** 5°. The open symbols denote the measured transition locations with TC (□) and TSP (◇). The dashed lines of subfigure (c) denote the disturbance frequency isolines corresponding to the medium grid while the colors correspond to the fine grid.

amplify at the upstream locations, where a benign local thickening of the boundary layer develops, becomes the most amplified disturbances along the length of the cone. They morph into the streak instabilities as the shear layer of the vortical structure forms and strengthens. The same scenario was found for the secondary instability of crossflow vortices over a circular cone at angle of attack [39, 40], the streak instability of the vortical structure over the minor axis plane of an elliptic cone [38], or the streak instability of the BOLT geometry at flight conditions [41].

To illustrate how the Mack mode evolution along the leeward side changes with angle of attack, Fig. 6 shows the N-factor curves for the leading frequencies and the N-factor envelopes for $AoA = 0^\circ$ and the selected angles of attack. The comparison of the Mack mode curves for $AoA = 0^\circ$ and 1° shown in Figs. 6(a) and 6(b), respectively, shows a significant effect on the instability properties. The boundary layer over the leeward side becomes unstable to Mack mode disturbances upstream of $x = 0.4$ m, while the first unstable Mack mode is found at $x = 0.62$ m for the $AoA = 0^\circ$ case. The measured transition location correlates with $N_E = 1.5$ as it moves upstream with the angle of attack increase. However, the N-factor values for the $AoA = 1^\circ$ case becomes lower than those of the $AoA = 0^\circ$ case for $x > 1.1$ m. Furthermore, Fig. 6(b) shows the N-factor envelope of planar Mack modes computed with conventional PSE along the leeward ray. The PSE overpredicts the amplification of Mack modes with respect to the plane-marching PSE, due to the assumption of azimuthal homogeneity. Figure 7(a) shows the evolution of the Mack mode disturbance with $f = 80$ kHz over the leeward side for $AoA = 1^\circ$. The contours of normalized streamwise velocity perturbation show that the Mack mode is localized around the leeward ray. The N-factor curves for $AoA = 3^\circ$ and $AoA = 5^\circ$ shown in Figs. 6(c) and 6(d) also initially correspond to Mack mode disturbances localized around the leeward ray, but they morph into streak instabilities as the detached three-dimensional shear layers of the vortical structures strengthen, leading to a large amplification of the disturbances that reach $N_E = 10$ and $N_E = 14$ for $AoA = 3^\circ$ and 5°. Furthermore, Fig. 6(c) shows the N-factor envelope based on the conventional (line marching) PSE along the leeward ray of the $AoA = 3^\circ$ case. Similar to the $AoA = 1^\circ$ case of Fig. 6(b), the PSE overpredicts the amplification of the Mack mode, but for the $AoA = 3^\circ$ case, it fails to predict the continuous amplification of the disturbance along the length of the cone. The reason for this difference is that the peak of the disturbances moves away from the leeward ray for $x > 0.7$ m as seen in the evolution of the streamwise velocity disturbance with $f = 45kHz$ for the $AoA = 3^\circ$ case shown in Fig. 7(b). The disturbance peak gradually moves from the inside of the boundary layer at $x = 0.4$ m toward the top of the vortical structure where the strong shear layer forms.

C. Linear Nonmodal Analysis

The previous results have shown that the modal amplification of the Mack mode waves yields a low N-factor value of $N_E = 1.5$ at the measured transition location for $AoA = 0^\circ$, which is deemed rather small to lead to transition onset even in a noisy facility. Therefore, the nonmodal instability characteristics of stationary and traveling, planar and oblique disturbances are investigated with HLNSE.

Figure 8 shows the contours of the energy gain as a function of the disturbance frequency and azimuthal wavenumber for the zero degrees angle of attack configuration. Results are presented for two different transient growth intervals with inflow locations of $\xi_0 = 0.2$ m (Figs. 8(a)) and $\xi_0 = 0.8$ m (8(b)), respectively, and a fixed outflow station corresponding to the measured transition location of $\xi_1 = 1.037$ m. Similar to the earlier results for blunt cones at Mach 6 and zero degrees angle of attack [10] for an optimization interval that begins near the nose, the maximum energy gain in Fig. 8(a) is achieved by a stationary ($f = 0$ kHz), three-dimensional perturbation. This stationary disturbance corresponds to the three-dimensional streaks studied by Paredes et al. [7]. There is an additional peak in the energy gain contours that corresponds to planar waves ($m = 0$) with a frequency of $f = 150$ kHz and an energy gain of $N_E = 3.9$. A significant range of planar and oblique traveling disturbances across the (f, m) spectrum are found to support appreciably large amplification factors of $N_E = 3.5 - 5$. These disturbances were also found for a Mach 6 configuration in Ref. [10] and were shown to amplify within the entropy layer region beyond the boundary-layer edge. They are initially tilted against the flow direction and increase in magnitude while their structure rotates downstream. The energy amplification is mainly attributed to the temperature perturbation within the entropy layer, where there exists a gradient in the mean flow temperature.

The spectrum of the optimal energy gain corresponding to the downstream inflow location of $\xi_0 = 0.8$ m in Fig. 8(b) shows the signature of the Mack mode disturbances in the form of a distinct amplification lobe for planar disturbances with a peak at $f = 180$ kHz and $N_E = 4$. Therefore, the nonmodal energy amplification reached by optimal disturbances is significantly larger than the purely modal amplification that yields $N_E = 1.5$ at the same location of $\xi = 1.037$ m. To illustrate the effect of the initial optimization location on the disturbance evolution, Fig. 9(a) shows the evolution of the energy gain in terms of $N_E = 0.5 \log(G_E)$ with selected ξ_0 and fixed $\xi_1 = 1.037$ m for a planar wave with $f = 180$

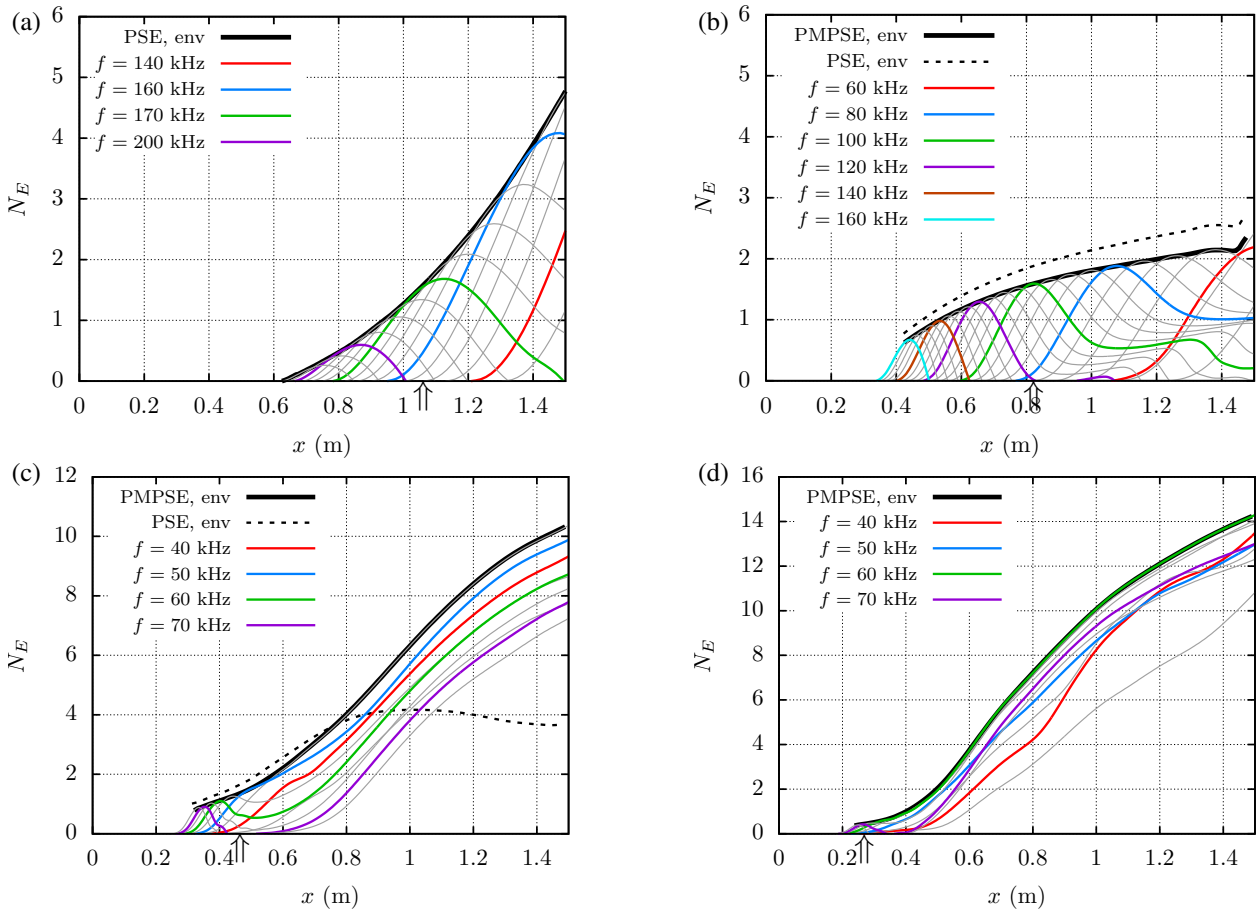

Fig. 6 N-factor contours of Mack mode instability for the (a) $AoA = 0°$ and along the leeward side for (b) $AoA = 1°$, (c) $3°$, (d) $5°$. The arrows denote the measured transition locations with TC. PMPSE refers to plane-marching PSE

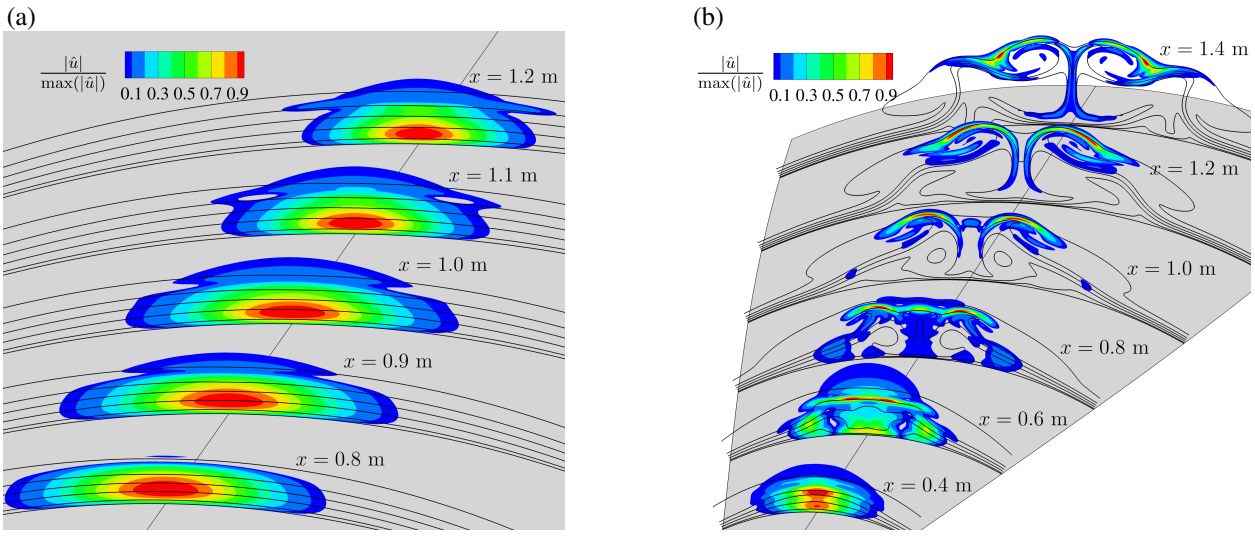

Fig. 7 Contours of streamwise velocity magnitude perturbation normalized with the local maximum and isolines of basic state streamwise velocity. (a) $AoA = 1°$ and $f = 80$ kHz, and (b)$AoA = 3°$ and $f = 45$ kHz.

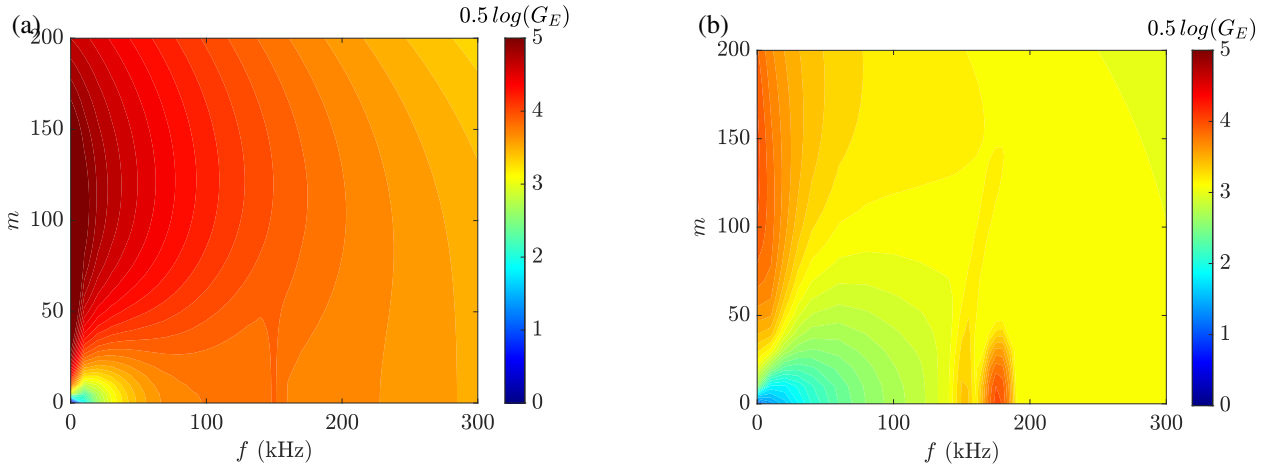

Fig. 8 Contours of $0.5\log(G_E)$ computed with HLNSE in the azimuthal wavenumber versus frequency plane for the cone at zero degrees angle of attack. The initial optimization location is selected at (a) $\xi_0 = 0.2$ m and (b) $\xi_0 = 0.8$ m. The final optimization location is selected at the measured transition location $\xi_1 = 1.037$ m.

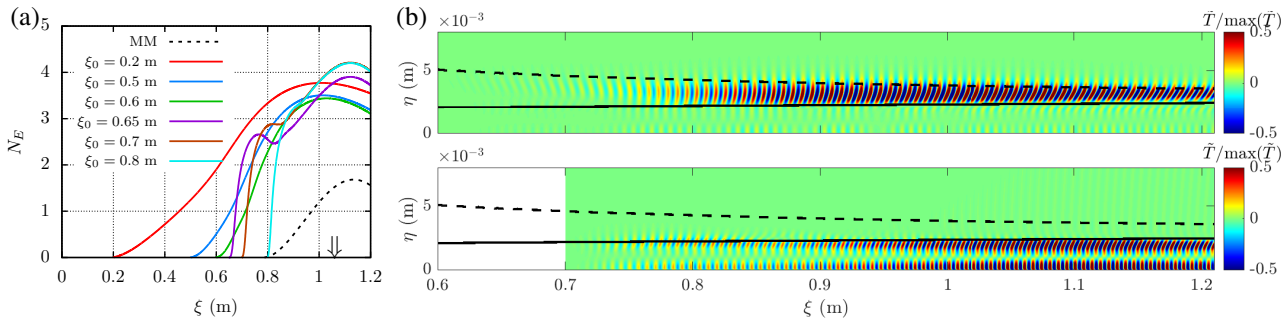

Fig. 9 (a) Evolution of $N_E = 0.5\log(G_E)$ computed with HLNSE for $f = 180$ kHz and $m = 0$ for selected initial optimization locations for the cone at zero degrees angle of attack. (b) Normalized contours of temperature perturbation for $\xi_0 = 0.6$ m and $\xi_0 = 0.7$ m. The final optimization location is selected at the measured transition location $\xi_1 = 1.037$ m.

kHz, as well as the N-factor of the planar Mack mode with $f = 180$ kHz. The peak amplitude gain is seen to decrease slightly when the initial location ξ_0 is increased from $\xi = 0.2$ m to $\xi = 0.6$ m. For $\xi_0 = 0.65$ m, the N_E curve has a nonmonotonic behavior and the curve shape matches that of the modal amplification of Mack mode instabilities but has higher values of amplification in comparison with the purely modal growth. As ξ_0 approaches the neutral location for the Mack mode waves, the optimal energy gain reaches a maximum of $N_E \approx 4$. Figure 9(b) shows the evolution of the disturbance temperature for $\xi_0 = 0.6$ m and $\xi_0 = 0.7$ m. The disturbance shape changes from an entropy layer disturbance that is confined to the band between the edges of the boundary layer and the entropy layer for $\xi_0 = 0.6$ m to a Mack mode disturbance that is located inside the boundary layer for $\xi_0 = 0.7$ m. Therefore, the nonmodal analysis shows that nonmodal entropy-layer disturbances and Mack mode disturbances can coexist at the measured transition location.

IV. Summary and Concluding Remarks

The present work investigated the modal and nonmodal instability characteristics of a 1.5 m long, 7° half-angle cone with a relatively blunt nosetip radius of 9.525 mm for selected angles of attack and freestream conditions from the experiments conducted by Marineau et al. [5] and Moraru [15] in the Air Force Arnold Engineering Development Complex (AEDC) Hypervelocity Wind Tunnel 9 at Mach 10.

Results are presented for a freestream Mach number of 9.79 and a freestream unit Reynolds number of 17.1×10^6 m^{-1}, for angles of attack equal to 0°, 1°, 3° and 5°, respectively. The laminar basic states are calculated by solving the full Navier-Stokes equations. The blunted nosetip results in a thick entropy layer that appreciably modifies the

three-dimensional boundary layer with respect to that over a sharp cone. The divergence of the streamlines from the windward side to the leeward side leads to a thickening of the boundary layer along the side of the cone and the formation of a vortical structure along the leeward side. As the angle of attack increases, the entropy-layer swallowing location along the windward ray is found to move upstream.

The modal instability analysis is performed by using PSE marching along inflection lines for stationary crossflow instabilities and along streamlines to study the amplification of traveling, planar, Mack-mode disturbances. In addition, plane-marching PSE are used along the leeward side to study the amplification of disturbances supported by the vortical structure. Results indicate that the maximum crossflow N-factors along the measured transition fronts at 1° and 3° angles of attack are less than 2 and less than 5, respectively. Thus, stationary crossflow instability is not likely to be the dominant transition mechanism at these conditions. However, stationary crossflow amplification is predicted to become more significant at angles of attack equal to or larger than 5 degrees. The predicted effect of the angle of attack on the Mack mode amplification agrees with the trend of the measured transition front. An important finding is that the Mack mode waves are destabilized along the windward side as a consequence of the upstream movement of the entropy-layer swallowing location with an increase in the angle of attack. Computations also indicate that the Mack mode N-factor at the measured transition locations increases with an increasing angle of attack. As a result of the boundary-layer thinning at the higher angles of attack, the frequency of the most amplified Mack mode disturbance at the transition location is also predicted to increase in relation to the dominant frequencies at the lower angles of attack. As one moves from the windward to the leeward symmetry plane, the accompanying shift in transition location approximately follows the locus of a constant Mack mode N-factor up to a certain distance from the leeward side, where a significantly earlier onset of transition within the localized vortical structure leads to the formation of a narrow turbulent wedge centered on the leeward ray. The plane-marching PSE analysis along the leeward side confirmed that, similar to earlier computations for centerline transition on the HIFiRE-5b elliptic cone, the dominant disturbances are initiated as localized Mack modes within the narrow azimuthal region of increased boundary-layer thickness near the leeward ray and that these disturbances morph into streak instabilities as the detached three-dimensional shear layer becomes stronger at angles of attack equal to 3 and 5 degrees. However, the N-factor values at the measured transition locations along the leeward side remain lower than $N = 2$ for the current configurations. A reduction in the transition N-factor is anticipated for the AEDC experiments because of the higher amplitudes of freestream disturbances relative to those expected during the HIFiRE-5b flight; however, such strikingly low values of the N-factor along the leeward ray were not anticipated and further work is necessary to determine their significance.

The nonmodal analysis for the blunt cone at zero degrees angle of attack showed a significant amplification of nonmodal disturbances across the frequency and azimuthal wavenumber spectrum that peak within the entropy layer and above the boundary-layer edge. The effect of the initial optimization location was investigated with a fixed final optimization location at the measured transition location. The nature of the optimal disturbances is found to change from entropy-layer disturbances to Mack mode disturbances as the inflow location from the spatial interval used for optimization approaches the neutral location of the Mack mode waves. Therefore, the analysis indicates that both nonmodal entropy-layer disturbances and modal Mack mode waves can coexist at the measured transition location. Furthermore, the optimal growth analysis indicates peak N-factor values of $N \approx 4$ at the measured transition location, i.e., more than twice the N-factor values based on modal growth alone.

Acknowledgments

This material is based upon research supported in part by the U. S. Office of Naval Research under award number N00014-20-1-2261 and in part by the Hypersonic Technology Project (HTP) under the Aeronautics Research Mission Directorate (ARMD). The computational resources supporting this work were provided by the DoD High Performance Computing Modernization Program, the NASA High-End Computing (HEC) Program through the NASA Advanced Supercomputing (NAS) Division at Ames Research Center and the LaRC K-Midrange Cluster at Langley Research Center. The authors would like to thank Dr. Marineau, Dr. Schneider and Mr. Moraru for technical discussions related to this topic. The authors are also thankful to Mr. Jeffery White and Dr. Robert Baurle for their generous advice concerning the VULCAN-CFD computations described in this paper.

References

[1] Schneider, S., "Hypersonic Laminar-Turbulent Transition on Circular Cones and Scramjet Forebodies," *Progress in Aerospace Sciences*, Vol. 40, 2004, pp. 1–50. doi:10.1016/j.paerosci.2003.11.001.

[2] Stetson, K., "Nosetip Bluntness Effects on Cone Frustum Boundary Layer Transition in Hypersonic Flow," AIAA Paper 83-1763, 1983. doi:10.2514/6.1983-1763.

[3] Malik, M., Spall, R., and Chang, C.-L., "Effect of Nose Bluntness on Boundary Layer Stability and Transition," AIAA Paper 90-0112, 1990. doi:10.2514/6.1990-112.

[4] Kufner, E., Dallmann, U., and Stilla, J., "Instability of Hypersonic Flow Past Blunt Cones - Effects of Mean Flow Variations," AIAA Paper 93-2983, 1993. doi:10.2514/6.1993-2983.

[5] Marineau, E., Moraru, C., Lewis, D., Norris, J., Lafferty, J., Wagnild, R., and Smith, J., "Mach 10 Boundary-Layer Transition Experiments on Sharp and Blunted Cones," AIAA Paper 2014-3108, 2014. doi:10.2514/6.2014-3108.

[6] Jewell, J., and Kimmel, R., "Boundary Layer Stability Analysis for Stetson's Mach 6 Blunt Cone Experiments," *Journal of Spacecraft Rockets*, Vol. 54, No. 1, 2017, pp. 258–265. doi:10.2514/1.A33619.

[7] Paredes, P., Choudhari, M., Li, F., Jewell, J., Kimmel, R., Marineau, E., and Grossir, G., "Nosetip Bluntness Effects on Transition at Hypersonic Speeds: Experimental and Numerical Analysis," *Journal of Spacecraft Rockets*, Vol. 56, No. 2, 2019. doi:10.2514/1.A34277.

[8] Jewell, J., Kennedy, R., Laurence, S., and Kimmel, R., "Transition on a Variable Bluntness 7-Degree Cone at High Reynolds Number," AIAA Paper 2018-1822, 2018. doi:10.2514/6.2018-1822.

[9] Cook, D., Thome, J., Brock, J., Nichols, J., and Candler, G., "Understanding Effects of Nose-Cone Bluntness on Hypersonic Boundary Layer Transition using Input-Output Analysis," AIAA Paper 2018-0378, 2018. doi:10.2514/6.2018-0378.

[10] Paredes, P., Choudhari, M., Li, F., Jewell, J., and Kimmel, R., "Nonmodal Growth of Traveling Waves on Blunt Cones at Hypersonic Speeds," *AIAA Journal*, Vol. 57, No. 11, 2019. doi:10.2514/1.J058290.

[11] Paredes, P., Choudhari, M., and Li, F., "Mechanism for Furstum Tranistion over Blunt Cones at Hypersonic Speeds," *Journal of Fluid Mechanics*, Vol. 894, 2020, p. A22. doi:10.1017/jfm.2020.261.

[12] Muir, J., and Trujillo, A., "Experimental Investigation of the Effects of Nose Bluntness, Free-Stream Unit Reynolds Number, and Angle of Attack on Cone Boundary Layer Transition at a Mach Number of 6," AIAA Paper 72-0216, 1972. doi:10.2514/6.1972-216.

[13] Stetson, K., "Effect of Bluntness and Angle of Attack on Boundary Layer Transition on Cones and Biconic Configurations," AIAA Paper 79-0269, 1979. doi:10.2514/6.1979-269.

[14] Holden, M., "Experimental Studies of the Effects of Asymmetric Transition on the Aerothermal Characteristics of Hypersonic Blunted Slender Cones," AIAA Paper 85-0325, 1985. doi:10.2514/6.1985-325.

[15] Moraru, C., "Hypersonic Boundary-Layer Transition Measurements at Mach 10 on a Large Seven-Degree Cone at Angle of Attack," Master's thesis, Purdue University, 2015.

[16] Stetson, K., "Hypersonic Boundary Layer Transition Experiments," AFWAL-TR-80-3062, 1980.

[17] Swanson, E., and Schneider, S., "Boundary-Layer Transition on Cones at Angle of Attack in a Mach-6 Quiet Tunnel," AIAA Paper 2010-1062, 2010. doi:10.2514/6.2010-1062.

[18] Willems, S., Gülhan, A., Juliano, T., and Schneider, S., "Laminar to Turbulent Transition on the HIFiRE-1 Cone at Mach7 and High Angle of Attack," AIAA Paper 2014-0428, 2014. doi:10.2514/6.2014-0428.

[19] Li, F., Choudhari, M., Chang, C., and White, J., "Analysis of Instabilities in Non-Axisymmetric Hypersonic Boundary Layers over Cones," AIAA Paper 2010-4643, 2010. doi:10.2514/6.2010-4643.

[20] Li, F., Choudhari, M., Chang, C., White, J., Kimmel, R., Adamczak, D., Borg, M., Stanfield, S., and Smith, M., "Stability Analysis for HIFiRE Experiments," AIAA Paper 2012-2961, 2012. doi:10.2514/6.2012-2961.

[21] Tokugawa, N., Choudhari, M., Ishikawa, H., Fujii, K., Atobe, T., Li, F., Chang, C.-L., and White, J., "Pressure Gradient Effects on Supersonic Transition over Axisymmetric Bodies at Incidence," *AIAA Journal*, Vol. 53, No. 12, 2015, pp. 3737–3751. doi:10.2514/1.J054070.

[22] Oliviero, N., Kocian, T., Moyes, A., and Reed, H., "EPIC:NPSE Analysis of Hypersonic Crossflow Instability on Yawed Straight Circular Cone," AIAA Paper 2015-2772, 2015. doi:10.2514/6.2015-2772.

[23] Tufts, M., Gosse, R., and Kimmel, R., "Parabolized Stability Equation Analysis of Crossflow Instability on HIFiRE-5b Flight Test," *Journal of Spacecraft Rockets*, Vol. 55, No. 6, 2018, pp. 1369–1378. doi:10.2514/1.A34149.

[24] Moyes, A., and Reed, H., "Preflight Boundary-Layer Stability Analysis of BOLT Geometry," *Journal of Spacecraft Rockets*, Vol. 58, No. 1, 2021, pp. 78–89. doi:10.2514/1.A34792.

[25] Paredes, P., "Advances in Global Instability Computations: from Incompressible to Hypersonic Flow," Ph.D. thesis, Universidad Politécnica de Madrid, 2014.

[26] Paredes, P., Hanifi, A., Theofilis, V., and Henningson, D., "The Nonlinear PSE-3D Concept for Transition Prediction in Flows With a Single Slowly-Varying Spatial Direction," *Procedia IUTAM*, Vol. 14C, 2015, pp. 35–44. doi:10.1016/j.piutam.2015.03.021.

[27] Paredes, P., Choudhari, M., and Li, F., "Instaiblity Wave-Streak Interactions in a Supersonic Boundary Layer," *Journal of Fluid Mechanics*, Vol. 831, 2017, pp. 524–553. doi:10.1017/jfm.2017.630.

[28] Chu, B.-T., "On the Energy Transfer to Small Disturbances in Fluid Flow (PART I)," *Acta Mechanica*, Vol. 1, No. 3, 1956, pp. 215–234. doi:10.1007/BF01387235.

[29] Mack, L. M., "Boundary Layer Stability Theory," Tech. Rep. Jet Propulsion Laboratory Report 900-277, California Institute of Technology, Pasadena, CA, 1969.

[30] Hanifi, A., Schmid, P., and Henningson, D., "Transient Growth in Compressible Boundary Layer Flow," *Physics of Fluids*, Vol. 8, 1996, pp. 826–837. doi:10.1063/1.868864.

[31] Paredes, P., Choudhari, M., Li, F., and Chang, C.-L., "Optimal Growth in Hypersonic Boundary Layers," *AIAA Journal*, Vol. 54, No. 10, 2016, pp. 3050–3061. doi:10.2514/1.J054912.

[32] Hermanns, M., and Hernández, J., "Stable High-Order Finite-Difference Methods Based on Non-Uniform Grid Point Distributions," *International Journal for Numerical Methods in Fluids*, Vol. 56, 2008, pp. 233–255. doi:10.1002/fld.1510.

[33] Paredes, P., Hermanns, M., Le Clainche, S., and Theofilis, V., "Order 10^4 Speedup in Global Linear Instability Analysis using Matrix Formation," *Computer Methods in Applied Mechanics and Engineering*, Vol. 253, 2013, pp. 287–304. doi:10.1016/j.cma.2012.09.014.

[34] Paredes, P., Gosse, R., Theofilis, V., and Kimmel, R., "Linear Modal Instabilities of Hypersonic Flow over An Elliptic Cone," *Journal of Fluid Mechanics*, Vol. 804, 2016, pp. 442–466. doi:10.1017/jfm.2016.536.

[35] Litton, D., Edwards, J., and White, J., "Algorithmic Enhancements to the VULCAN Navier-Stokes Solver," AIAA Paper 2003-3979, 2003. doi:10.2514/6.2003-3979.

[36] Roy, C., and Blottner, F., "Review and Assessment of Turbulence Models for Hypersonic Flows," *Progress in Aerospace Sciences*, Vol. 42, 2006, pp. 469–530. doi:10.1016/j.paerosci.2006.12.002.

[37] Choudhari, M., Chang, C.-L., Jentink, T., Li, F., , Berger, K., Candler, G., and Kimmel, R., "Transition Analysis for the HIFiRE-5 Vehicle," AIAA Paper 2009-4056, 2009.

[38] Choudhari, M., Li, F., and Paredes, P., "Streak Instabilities on HIFiRE-5 Elliptic Cone," AIAA Paper 2020-0828, 2020. doi:10.2514/6.2020-0828.

[39] Li, F., Choudhari, M., Paredes, P., and Duan, L., "High-Frequency Instabilities of Stationary Crossflow Vortices in a Hypersonic Boundary Layer," *Physical Review Fluids*, Vol. 1, 2016, pp. 053603–1–32. doi:10.1103/PhysRevFluids.1.053603.

[40] Choudhari, M., Li, F., and Paredes, P., "Nonlinear Evolution and Breakdown of Azimuthaly Compact Crossflow Vortex Pattern over a Yawed Cone," AIAA Paper 2018-1823, 2018. doi:10.2514/6.2018-1823.

[41] Li, F., Choudhari, M., and Paredes, P., "Streak Instability Analysis for BOLT Configuration," AIAA Paper 2020-3028, 2020. doi:10.2514/6.2020-3028.